Journal of Materials Chemistry A

RSC Publishing

PAPER

View Article Online
View Journal | View Issue

Cite this: J. Mater. Chem. A, 2013, 1, 3954

CO_2–expanded ethanol chemical synthesis of a Fe_3O_4@graphene composite and its good electrochemical properties as anode material for Li-ion batteries†

Linhai Zhuo,[ac] Yingqiang Wu,[acd] Lingyan Wang,[acd] Jun Ming,[acd] Yancun Yu,[ac] Xinbo Zhang*[b] and Fengyu Zhao*[ac]

Received 6th December 2012
Accepted 17th January 2013

DOI: 10.1039/c3ta01388j

www.rsc.org/MaterialsA

In this work, we have developed a new method to synthesize a Fe_3O_4@graphene (Fe_3O_4@GN) composite. First, the precursor was synthesized through the decomposition of ferric nitrate in the presence of graphene oxide in the mixed solvent of CO_2–expanded ethanol. Then, the precursor was converted to the Fe_3O_4@GN composite *via* thermal treatment in N_2 atmosphere. With the help of the CO_2–expanded ethanol, Fe_3O_4 nanoparticles were coated on the surface of GN completely and uniformly with high loading. However, it is difficult to load Fe_3O_4 particles onto the surface of GN and most of the Fe_3O_4 particles were deviated away from GN and aggregated to form larger units in pure ethanol. When used as anode for Li-ion batteries (LIBs), the Fe_3O_4@GN composite with a graphene content of 25 wt% synthesized in CO_2–expanded ethanol manifested excellent charge–discharge cycling stability and rate performance compared with the sample synthesized in ethanol. Such improved electrochemical performances should be attributed to the intimate contact between the GN and Fe_3O_4 nanoparticles in the composite. Since the present method does not need tedious pre-treatment, surfactant, or precipitate, it is a green or sustainable technology and the solvents could be recycled easily after simple phase separation. This facile method can be extended to the synthesis of other metal oxide composites, which are expected to have good performance as anode materials for LIBs and other applications.

Introduction

Among the various electrochemical storage technologies, rechargeable lithium ion batteries (LIBs), which can deliver high energy density and power density with good cyclability, have been drawing wide attention in both the scientific and industrial fields.[1] The widely used LIBs for portable electronics at present use lithium transition metal oxides as cathodes and graphite as anode.[2,3] However, graphite has an inherent limitation with a theoretical gravimetric capacity estimated at 372 mA h g^{-1}.[3,4] In order to satisfy the high demand requested from some new applications such as vehicles and large energy storage devices, extensive efforts are in progress to find new electrode materials with higher gravimetric and volumetric capacity. For this purpose, transition metal oxides have been studied widely as possible alternatives to carbonaceous anode materials because they can exhibit 2–3 times larger capacities than graphite.[5–9] Among these metal oxides, Fe_3O_4 is considered as one of the promising candidate materials because of its abundance, low cost, nontoxicity, and high theoretical reversible capacity (927 mA h g^{-1}).[10] However, the cyclability of pure Fe_3O_4 is poor due to its unsatisfactory electronic conductivity and the large volume expansion after repetitive charging and discharging, which causes the collapse of the active materials and the loss of electrical contact.[11–13] Therefore, the key to enhancing the cycling ability of Fe_3O_4 is to increase the electrical conductivity and decrease the pulverization induced by the volume change as well.[14–19]

To resolve these problems, many researchers are devoted to synthesizing nanostructured Fe_3O_4–carbon hybrid materials, which can not only absorb the internal volume changes during cycling, but also enhance the electronic conductivity of the composites.[20–22] Recently, graphene has attracted special attention due to its excellent electronic conductivity, mechanical properties and high surface area (theoretical value of 2630 m^2 g^{-1}), which provides opportunities for designing new

[a]State Key Laboratory of Electroanalytical Chemistry, Changchun Institute of Applied Chemistry, Chinese Academy of Sciences, Changchun 130022, China

[b]State Key Laboratory of Rare Earth Resource Utilizations, Changchun Institute of Applied Chemistry, Chinese Academy of Sciences, Changchun 130022, China. E-mail: xbzhang@ciac.jl.cn

[c]Laboratory of Green Chemistry and Process, Changchun Institute of Applied Chemistry, Chinese Academy of Sciences, Changchun 130022, China. E-mail: zhaofy@ciac.jl.cn; Fax: +86-431-85262410; Tel: +86-431-85262410

[d]University of the Chinese Academy of Sciences, Beijing 100049, China

† Electronic supplementary information (ESI) available. See DOI: 10.1039/c3ta01388j

functional composite materials through grafting the target materials onto graphene plates.[23–25] To date, Fe_3O_4 nanoparticles grafted on graphene as anode materials for LIBs have been reported by several research groups and showed promising electrochemical performances.[10,26–37] However, the reported synthesis methods always need surfactants or some highly viscous solvents to avoid the aggregation of the final nanoparticles. The introduction of these additional additives inevitably makes the solid–liquid separation more complex. Furthermore, it is still a challenge for Fe_3O_4 nanoparticles to be well adhered and homogeneously distributed on the surface of GN.[10,27,29,31,32,36]

Recently, searching for alternative methods to synthesize materials for LIBs appears to be very attractive. As a green and sustainable technology, supercritical carbon dioxide ($scCO_2$) is now drawing sustained interest in current scientific and industrial fields.[38,39] $ScCO_2$ is an attractive alternative to conventional solvents due to its environmentally friendly nature and unique features of tunable physical properties characterized by low viscosity, high diffusivity, and absence of surface tension.[40] Over the past decade, the synthesis of organic compounds using $scCO_2$ as solvent has been developed into an advantageous synthetic technique.[41] Recently, the specific properties of $scCO_2$ have been exploited for the synthesis of functional nanomaterials, especially in the field of inorganic and hybrid materials.[42–44] In this work, we present a new method to synthesize a Fe_3O_4@GN composite in CO_2–expanded ethanol (CE). With the help of the CE, Fe-salt nanoparticles were successfully deposited on the surfaces of graphene oxide (GO) *via* the decomposition of ferric nitrate at relatively low temperatures to form a Fe-salt@GO composite. After thermal treatment in N_2 atmosphere, the Fe-salt@GO composite was converted to a Fe_3O_4@GN composite. When used as anode for LIBs, the Fe_3O_4@GN composite with a graphene content of 25 wt% synthesized in CE manifested excellent charge–discharge cycling stability and rate performance. For elucidation of the efficiency of $scCO_2$, the sample was also prepared under the same conditions in pure ethanol without $scCO_2$ and the electrochemical properties were compared with those of the composite fabricated in CE.

Experimental section

Materials synthesis

All chemicals were used as received without further purification. $Fe(NO_3)_3 \cdot 9H_2O$ was purchased from Beijing Chemical Works. Natural graphite powder was purchased from Sinopharm Chemical Reagent Co.,Ltd. Commercial Fe_3O_4 was purchased from Shenyang No.5 Reagent Factory.

GO was prepared from purified natural graphite powder according to the improved method.[45] GO (20 mg) was diluted with absolute alcohol (5 mL) in a flask, and ultrasonicated for 120 min. 0.15 g $Fe(NO_3)_3 \cdot 9H_2O$ was added to the flask. Then the dispersion was loaded into a high-pressure vessel of 50 mL. The vessel was charged with CO_2 up to 10 MPa at 50 °C. Subsequently, it was moved into an oil bath and maintained at 120 °C for about 6 h. After it was cooled to ambient temperature, the vessel was slowly depressurized. After centrifugation, the intermediate compound was collected and then vacuum dried at 100 °C for 6 h. The intermediate compound deposited from precursors in CE is referred to as Fe-salt@GO-CE-20. After drying, the Fe-salt@GO-CE-20 composite was calcined in a tube furnace under N_2 atmosphere at 450 °C for 3 h to obtain the final product, which was designated as Fe_3O_4@GN-CE-20. Fe-salt@GO-CE-15 and Fe_3O_4@GN-CE-15 were also synthesized by the same method, in which the amount of GO was decreased to 15 mg. For comparison and elucidation of the efficiency of $scCO_2$, samples were also fabricated only using pure ethanol as solvent, and designated as Fe-salt@GO-E-20, and Fe_3O_4@GN-E-20, respectively.

Characterization

The phase structures were characterized with X-ray diffraction [XRD, Bruker D8 Advance diffractometer using Cu Kα radiation ($\lambda = 1.5418$ Å)]. The morphology of the materials was analyzed using a scanning electron microscope (SEM Hitachi S-4800). Transmission electron microscope (TEM) images were recorded on a Tecnai G20 operating at 200 kV for the detailed microstructure information of the sample. Thermal gravimetric analysis (TGA) was carried out using a TGA 2050 thermogravimetric analyzer. X-ray photoelectron spectra (XPS) were recorded on a PHI quantera SXM spectrometer with an Al Kα = 280.00 eV excitation source, where binding energies were calibrated by referencing the C1s peak (284.5 eV) to reduce the sample charge effect. N_2 adsorption/desorption isotherms were measured using a Micromeritics ASAP 2020 Analyzer (USA).

Electrochemical characterization

The electrochemical tests were measured using two-electrode 2025-type coin cells assembled in an argon-filled glove box. Lithium sheets served as the counter electrode and reference electrode, and a polypropylene film (Celgard-2300) was used as a separator. The electrolyte was a 1.0 M $LiPF_6$ solution in a mixture of EC–DMC (1 : 1 in volume). The working electrodes were prepared by a slurry coating procedure. The slurry consisted of 80 wt% active materials, 10 wt% acetylene black and 10 wt% polyvinylidene fluorides dissolved in *N*-methyl-2-pyrrolidinone. This slurry was spread on copper foil, which acted as a current collector. The electrodes were dried at 100 °C for 4 h in air, and then at 100 °C in vacuum for another 12 h and pressed. The weight of every electrode was weighed accurately using an electronic balance. The mass of the active materials was controlled in the range of 1–2 mg. Furthermore, the thickness of the electrode was measured by SEM. As can be seen from Fig. S1,† the thickness of the active materials was about 13 μm at a mass of 1.65 mg. Galvanostatic charge–discharge cycles were carried out on a battery tester between 0.01 and 3.00 V at various current densities on a NEWARE cell test instrument (Shenzhen Neware Electronic Co., China).

Results and discussion

Since the decomposition temperature of metal nitrates in CE is relatively low, the intermediate produced are usually

amorphous. From the XRD patterns of Fe-salt@GO-CE-20 (Fig. S1†), it is difficult to confirm the chemical structure because the intermediate was not well crystallized. Our recent work has investigated the chemical composition of the amorphous intermediate and the deposition reaction mechanism of hydrous inorganic metal salts in CE in detail.[46] Based on the previous results, the intermediate Fe-salt was speculated to be $Fe_x(OH)_y(NO_3)_z(CO_3)_m \cdot nH_2O$. After calcination at 450 °C in N_2 for 3 h, the Fe-salt@GO composite was converted to Fe_3O_4@GN composite. The XRD patterns of the Fe_3O_4@GN composites prepared in CE and pure ethanol are shown in Fig. 1a. The XRD patterns of the as-prepared nanocomposites match both the magnetite Fe_3O_4 (JCPDS card 75-0449) and the maghemite γ-Fe_2O_3 (JCPDS card 39-1346) structures because the XRD patterns of magnetite and maghemite are extremely similar.[29] In order to verify the chemical composition of the nanocomposites, XPS was measured in the region of 0–1200 eV. From the result of the high-resolution XPS spectrum of Fe_3O_4@GN-CE-20 shown in Fig. 1b, magnetite Fe_3O_4 was confirmed according to the typical characteristic peaks of Fe 2p3/2 and Fe 2p1/2 at 710.9 and 724.5 eV, respectively.[30]

GN could be burned away in air at high temperature, while bare Fe_3O_4 was stable in this temperature range.[27] TGA analysis for the composites was carried out in air to quantify the amount of GN in the composites. As seen from Fig. S3,† the weight loss over the temperature range from 40 to 200 °C might be due to the loss of residual water in the samples. Most of the weight loss of the nanocomposites occurred at about 300–500 °C, indicating the oxidation and decomposition of GN in air. According to the TGA analysis, the amount of GN was about 25% in the Fe_3O_4@GN-CE-20 and Fe_3O_4@GN-E-20 composites, and 17% in the Fe_3O_4@GN-CE-15 composite.

To investigate the morphologies of the samples, SEM and TEM images were collected for GO, Fe-salt@GO-CE-20 and Fe_3O_4@GN-CE-20 composites. Fig. S4† shows the SEM and TEM images of GO with wavy structures, which graphene intrinsically possesses. After deposition in CE, the SEM image of the Fe-salt@GO-20 showed that the two-dimensional GO sheets were well decorated with a thin layer of small nanoparticles (Fig. 2a). After thermal treatment in N_2 atmosphere, the high-resolution SEM image (Fig. 2b) indicated that the morphology of the final product (Fe_3O_4@GN-CE-20) was not changed. The microstructure of Fe_3O_4@GN-CE-20 was further characterized by TEM technique. The TEM image of Fe_3O_4@GN-CE-20 shown in Fig. 2c revealed that the Fe_3O_4 nanoparticles were distributed on the surface of GN in the form of individual particles in the range of 10–30 nm. There were no free Fe_3O_4 nanoparticles isolated from GN or vacancy on GN. Considering that ultrasonication was used during the preparation of the TEM specimen, the above observation also revealed that these Fe_3O_4 particles were firmly attached to the GN. The HRTEM image and the corresponding fast Fourier transform pattern (the inset image) are shown in Fig. 2d. The lattice fringes with *d*-spacings of 0.29 nm and 0.48 nm can be assigned to the (220) and (111) planes of cubic Fe_3O_4. Energy-dispersive X-ray spectroscopy elemental mapping was used to help understand the distribution of Fe_3O_4 particles and GN in the Fe_3O_4@GN-CE-20 composites. The Fe_3O_4 particles were homogeneously distributed in the composite as confirmed by the elemental distribution of iron, oxygen, and carbon shown in Fig. S5.† Furthermore, the effect of the amount of GO on the loading

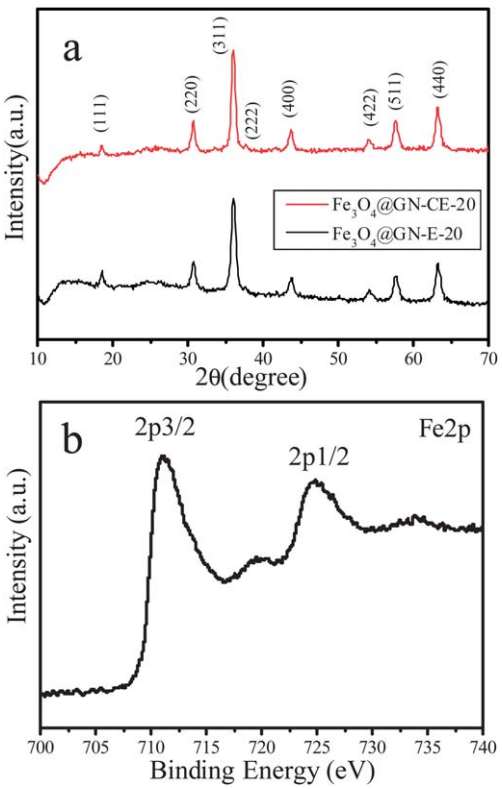

Fig. 1 (a) XRD patterns of the Fe_3O_4@GN composites prepared in different solvents. (b) Fe 2p core-level XPS spectrum of the Fe_3O_4@GN-CE-20 composite.

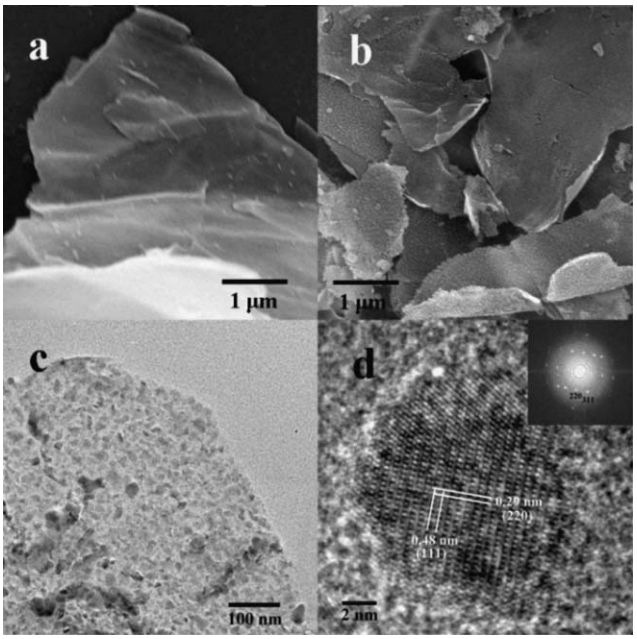

Fig. 2 SEM images of (a) Fe-salt@GO-CE-20 and (b) Fe_3O_4@GN-CE-20. (c) TEM image of Fe_3O_4@GN-CE-20. (d) High resolution TEM image of Fe_3O_4@GN-CE-20.

quality of Fe_3O_4 nanoparticles was also investigated. The SEM and TEM images of the Fe-salt@GO-CE-15 and Fe_3O_4@GN-CE-15 composites showed that there were two kinds of nanoparticles with different dimensions distributed on the surface of GO and GN (Fig. S6†). The small particles were about 10–30 nm in diameter, while the large ones were about 100 nm in diameter as observed in TEM images. This result can be explained by the fact that GO could provide nucleation sites, some larger particles were formed with less amount of GO at a constant concentration of $Fe(NO_3)_3 \cdot 9H_2O$.

The key effect of $scCO_2$ for the quasi-uniform coverage of GN was also clarified by performing a control experiment in ethanol without CO_2. As shown in Fig. 3a, SEM examination of the Fe-salt@GO-E-20 composite showed that the most of the Fe-salt particles were aggregated into larger units, and only a few particles were loaded on GO. After the composite was calcined in N_2, the obtained sample also showed a poor dispersion and an agglomeration of the final particles (Fig. 3b). The above control experiments indicate the importance of $scCO_2$ in the formation of the hybrid materials. In this work, compressed CO_2 was introduced into the vessel and dissolved into ethanol accompanying volume expansion of the solutions. The introduction of CO_2 altered the polarity of the ethanol, which was beneficial to the precipitation of the ferric salt. During the synthesis, Fe^{3+} was first captured by hydroxyl, carboxyl or epoxy groups on the GO by coordination, and the adsorbed species acted as preferential nucleation sites, at which the generated Fe-salt nanoparticles nucleated and grew to form larger particles. Meanwhile, $scCO_2$ as an anti-solvent reduced the solvent strength caused by hydroxyls originating from ethanol and crystal water, which could reduce the aggregation of the final particles.[40] Moreover, owing to the special properties of $scCO_2$, like the low viscosity, high mass transfer rate and absence of surface tension, the metal oxide nanoparticles produced in $scCO_2$ tended to deposit onto the surfaces of GO. As a consequence, GO was readily loaded with a dense and uniform layer of small nanoparticles in CE. However, for pure ethanol, the existence of surface tension, hydroxyls, and low diffusivity, which strongly limit the ability to disperse and transfer generated solid intermediates to grow on the surface of vthe substrate, resulted in the guest components being poor adhered on GO or crystallized and aggregated freely in solution.

N_2 sorption measurements were conducted to investigate the Brunauer–Emmett–Teller (BET) specific surface areas and porous structures of the Fe_3O_4@GN-CE-20 and Fe_3O_4@GN-E-20 composites (Fig. S7†). The BET surface areas of the Fe_3O_4@GN-CE-20 and Fe_3O_4@GN-E-20 were 116 $m^2\ g^{-1}$ and 155 $m^2\ g^{-1}$, respectively, which were much higher than the value of commercial Fe_3O_4 reported previously.[10,31] The pore volume was 0.254 $cm^3\ g^{-1}$ for Fe_3O_4@GN-CE-20 and 0.634 $cm^3\ g^{-1}$ for Fe_3O_4@GN-E-20. It is worth noting that the surface area and the pore volume of Fe_3O_4@GO-E-20 were higher than those of Fe_3O_4@GO-CE-20. The result may be ascribed to the low loading of Fe_3O_4 nanoparticles on the surfaces of GN and the dissociated and aggregated Fe_3O_4 nanoparticles in the Fe_3O_4@GN-E-20 composite which served as spacers to prevent the composite from restacking.[31,47] The porous structure of the composites could act as buffering spaces against the volume change of Fe_3O_4 particles during the cycles, and facilitate lithium ions and electrolyte molecules to access to active sites.[10,29,31]

To identify all of the electrochemical reactions, cyclic voltammetry (CV) was conducted with Fe_3O_4@GN-CE-20 composite and commercial Fe_3O_4 as the anodes at ambient temperature based on the half cell configuration. The cells were studied in the potential range of 0.01–3.0 V *vs.* Li/Li^+ at a scan rate of 0.1 mV s^{-1}. The cyclic voltammograms (CVs) of the Fe_3O_4@GN-CE-20 and commercial Fe_3O_4 electrodes are shown in Fig. 4a and b. The first cathodic scans of the two materials presented two peaks located in the range from 0.6 V to 0.8 V, which could be attributed to the reduction of Fe_3O_4 to Fe^0 and the irreversible decomposition of the electrolyte.[27] After the first scan, the CV patterns of Fe_3O_4@GN-CE-20 and commercial Fe_3O_4 showed one cathodic peak at ~0.75 V. This cathodic peak intensity of Fe_3O_4@GN-CE-20 was increased slightly with increasing cycling number, which could be attributed to the gradual activation of the electrode in the first few cycles. Meanwhile, two peaks were recorded at about 1.6 and 1.8 V in the anodic process of Fe_3O_4@GN-CE-20, corresponding to the oxidation of Fe^0 to Fe_3O_4 during the anodic process.[27] However, the pair of anodic peaks was not visible in commercial Fe_3O_4. Different from commercial Fe_3O_4, the anodic peak current and the integrated area intensity of Fe_3O_4@GN-CE-20 were nearly unchanged from cycle to cycle, indicating that there was almost no capacity loss during charging. The CV measurements therefore indicated good electrochemical activity and stability of the Fe_3O_4@GN-CE-20 composite compared with commercial Fe_3O_4. In contrast, as shown in Fig. 4b, the gradual decrease of the redox peak intensity and the integrated area implied worse electrochemical activity and stability of commercial Fe_3O_4.

The electrochemical performances of the Fe_3O_4@GN-CE-20 and Fe_3O_4@GN-E-20 nanocomposites were evaluated by galvanostatic charge–discharge tests. Fig. 4c and d show the charge–discharge voltage profiles of the cells for the first two cycles at a current rate of 200 mA g^{-1} and the 3rd and 100th cycle at a current rate of 1 A g^{-1}. In the discharge curves of the first cycle, both the samples exhibited a typical plateau at around 0.8 V, corresponding to the formation of a solid–electrolyte interfacial (SEI) layer and the reaction of Fe_3O_4 with lithium to form amorphous Li_2O and Fe^0. The first discharge and charge capacities for the Fe_3O_4@GN-CE-20 composite (Fig. 4c) were 1280 mA h g^{-1} and 941 mA h g^{-1}, respectively. The discharge

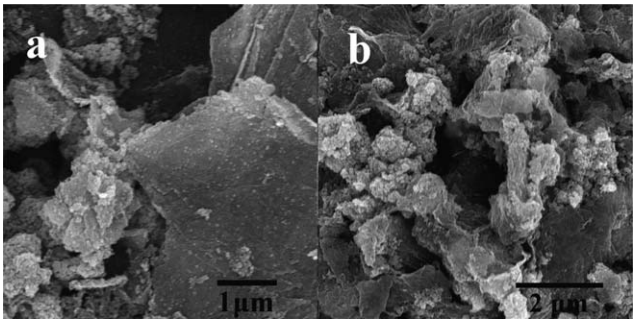

Fig. 3 SEM images of (a) Fe-salt@GO-E-20 and (b) Fe_3O_4@GN-E-20 composites.

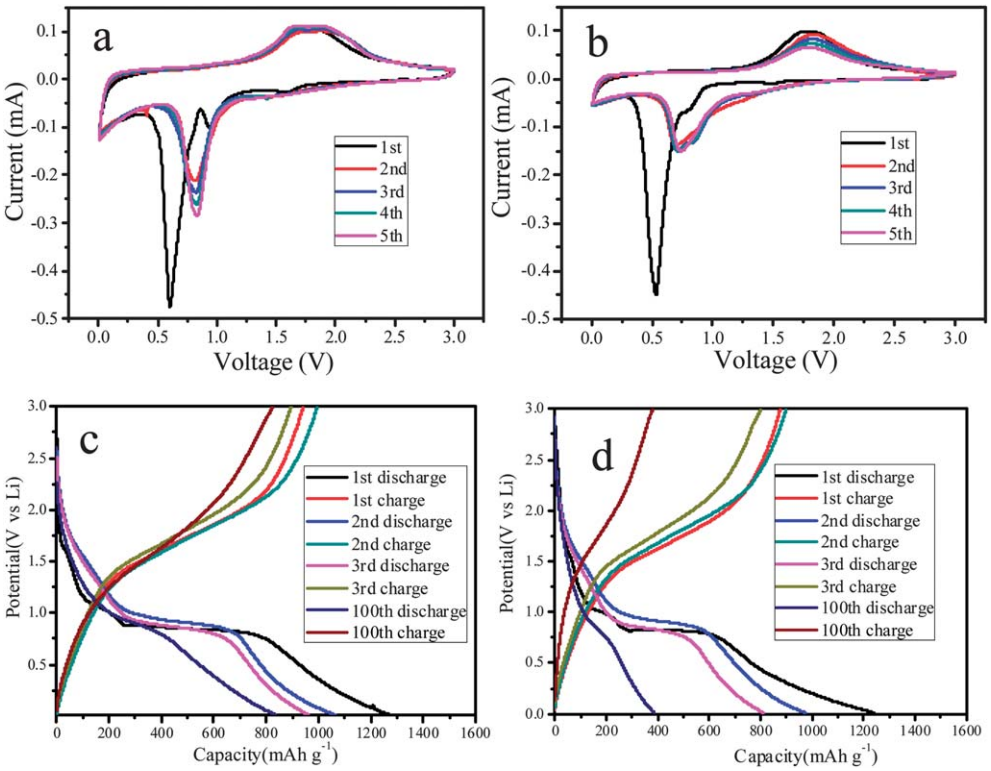

Fig. 4 Typical cyclic voltammograms of (a) Fe_3O_4@GN-CE-20 and (b) commercial Fe_3O_4 at a sweep rate of 0.1 mV s^{-1}. The 1st, 2nd, 3rd, and 100th charge–discharge voltage profiles of (c) Fe_3O_4@GN-CE-20 and (d) Fe_3O_4@GN-E-20.

capacities of composite at the 3rd cycle and at the 100th cycle were 965 mA h g^{-1} and 838 mA h g^{-1}, respectively. By contrast, the reversible capacity of the Fe_3O_4@GN-E-20 electrode (Fig. 4d) rapidly dropped to 370 mA h g^{-1} at the 100th cycle at a current rate of 1 A g^{-1}. The Coulombic efficiency for the Fe_3O_4@GN-CE-20 composite rises from 73.5% at the first cycle to 93.2% at the 2th cycle and 98.5% at the 100th cycle. The initial Coulombic efficiency of Fe_3O_4@GN-CE-20 was considerably higher than those of materials reported in the literature such as Fe_3O_4-Carbon-rGO (around 64%),[33] Fe_3O_4/GNSs-1 (55%),[31] GN-Fe_3O_4 (65.5%),[29] or Fe_3O_4-GNS (61.5%),[27] and equivalent to those of RGO-Fe_3O_4 nanocomposites (71%)[34] or Fe_3O_4/MSU-F-C-61 (71%).[48]

It has been reported that one mole of Fe_3O_4 has the ability to react with eight moles of Li ions through the conversion reaction: $Fe_3O_4 + 8Li^+ + 8e \leftrightarrow 4Li_2O + 3Fe$.[10] Based on this reaction, the theoretical capacity of Fe_3O_4 can be calculated to be 922 mA h g^{-1}. In addition, the largest reversible capacity for GN was 561 mA h g^{-1}. Therefore, the theoretical capacity of the Fe_3O_4@GN-CE-20 composite was 831 mA h g^{-1} (561 mA h g^{-1} × 0.25 + 922 mA h g^{-1} × 0.75). Fig. 5a shows a comparison of the charge–discharge cyclic performances for the bare GN, commercial Fe_3O_4, Fe_3O_4@GN-CE-20, Fe_3O_4@GN-CE-15, and Fe_3O_4@GN-E-20 composites. The cells were cycled at a current of 200 mA g^{-1} for the first two cycles and then cycled at a current of 1 A g^{-1} up to 100 cycles. The bare GN nanosheets had an initial discharge capacity of 1004 mA h g^{-1} and charge capacity of 561 mA h g^{-1} with a Coulombic efficiency of 55.8%. After 100 cycles, the charge capacity of GN dropped to 233 mA h g^{-1}. For commercial Fe_3O_4, there was a rapid fading of capacity due to severe pulverization after 100 cycles. In contrast with bare GN and commercial Fe_3O_4, Fe_3O_4@GN-CE-20 had a charge capacity of 826 mA h g^{-1} at the 100th cycle. Besides, it was found that the graphene content has a great effect on the electrochemical performance of the composite. As shown in Fig. 5a, with reduction of the graphene content, the Fe_3O_4@GN-CE-15 composite with 17 wt% graphene showed a decrease in cyclic performance compared with Fe_3O_4@GN-CE-20. This can be explained as follows: (i) the electrical conductivity of the composite decreased with decreasing of GN and (ii) larger Fe_3O_4 particles formed in the composite. The cycling performances of the composite prepared in ethanol were also tested. The first discharge and charge capacities for the Fe_3O_4@GN-E-20 composite were 1239 mA h g^{-1} and 875 mA h g^{-1}, respectively. After cycling up to 100 cycles, the charge capacity for Fe_3O_4@GN-E-20 was only 370 mA h g^{-1}. To further investigate and compare the electrochemical performances of Fe_3O_4@GN-CE-20 and Fe_3O_4@GN-E-20, the charge–discharge measurements for them were also carried out at various current densities. As shown in Fig. 5b, Fe_3O_4@GN-CE-20 also presented better rate performance than Fe_3O_4@GN-E-20. Even at a high current density of 5 A g^{-1}, the composite was still able to deliver a capacity of 460 mA h g^{-1}, about 40% of the initial capacity. However, the capacity of Fe_3O_4@GN-E-20 dropped dramatically to 40 mA h g^{-1} at this high rate, only 4% of the initial capacity. If the current changed from 5 A g^{-1} to 200 mA g^{-1}, the specific

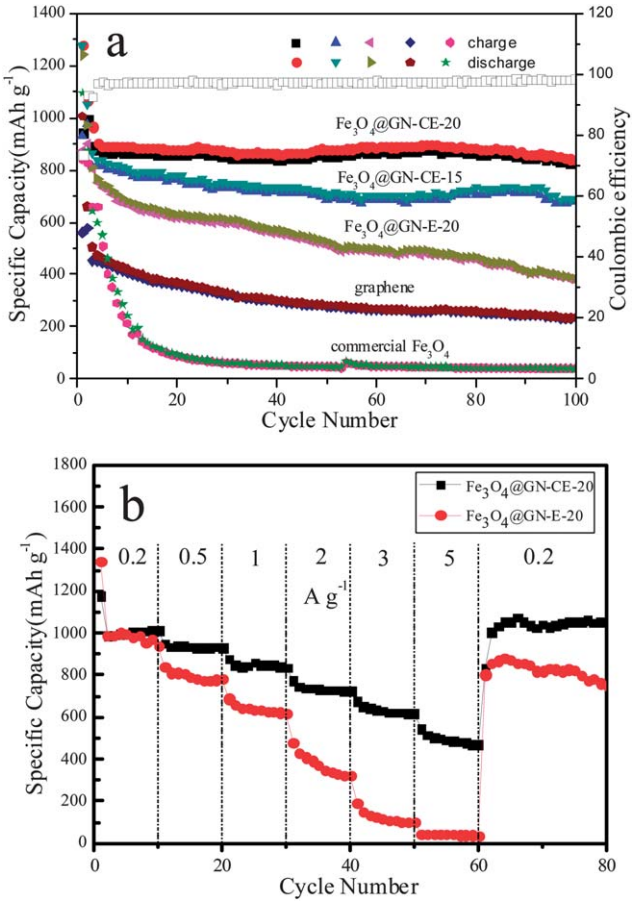

Fig. 5 (a) Cycling performances of the bare GN, commercial Fe_3O_4, Fe_3O_4@GN-CE-20, Fe_3O_4@GN-CE-15, and Fe_3O_4@GN-E-20 composites at a current of 200 mA g^{-1} for the first two cycles and then cycled at a current of 1 A g^{-1} up to 100 cycles. (b) Rate performances of the Fe_3O_4@GN-CE-20 and Fe_3O_4@GN-E-20 composites.

capacity of Fe_3O_4@GN-CE-20 could return to ~1000 mA h g^{-1} gradually, indicating high cycling stability. However, for Fe_3O_4@GN-E-20, when the current changed from 5 A g^{-1} to 200 mA g^{-1}, the gradual decreasing capacity implied worse stability of the composite.

The above results clearly showed that the reversible capacity, the Coulombic efficiency, cycling performance and the rate cycling behavior of the sample synthesized in CE were significantly improved in comparison with the sample synthesized in ethanol. In comparison with the recent studies on Fe_3O_4@graphene composites (Table S1†), Fe_3O_4@GN-CE-20 also showed good rate capability and better cycle stability. The better electrochemical performance of Fe_3O_4@GN-CE-20 can be attributed to the following aspects. (1) The presented method avoids the formation of dissociative particles in solution due to the unusual reaction media with such unique properties as low viscosity, high diffusivity, and absence of surface tension. (2) The presence of GN in the composite prevents Fe_3O_4 from agglomerating and enables a good dispersion of these nanoparticles over the surfaces of GN sheets. (3) The good mechanical flexibility of GN can readily absorb the massive volume expansion associated with a conversion reaction electrode. (4) The intimate contact between the GN sheets and Fe_3O_4 nanoparticles affords facile electron transport to ensure electrochemical activity. Compared with the Fe_3O_4@GN-E-20 composite, there was a similar amount of GN, lower BET surface area and pore volume for Fe_3O_4@GN-CE-20, but the electrochemical performance of Fe_3O_4@GN-CE-20 was still superior to that of Fe_3O_4@GN-E-20, which was mainly ascribed to the high loading of Fe_3O_4 on the GN in the composite.

Conclusions

In summary, we have developed a new method to grow Fe_3O_4 nanoparticles on GN through a simple low temperature chemical deposition in CO_2–expanded ethanol. The high loading and good adhesion of Fe_3O_4 nanoparticles on GN resulted from the unusual properties of $scCO_2$. The presented method is a green process without using any harmful solvents or precipitants and the solvent can be recycled after simple phase (gas–liquid–solid) separation. Furthermore, the present method avoids the long and tedious steps, such as repeated washing or filtering to remove the excessive precipitants, surfactants, or some highly viscous solvents. When used as anode material for LIBs, the Fe_3O_4@GN-CE-20 composite exhibited a higher reversible capacity, better cycle and rate performance compared with the sample synthesized in pure ethanol. The strategy described in this paper is a green or sustainable technology, which could be easily extended to the synthesis of a wide range of functional nanomaterials.

Acknowledgements

This work was financially supported by the One Hundred Talent Program of CAS and NSFC (21273222).

Notes and references

1 M. Armand and J. M. Tarascon, *Nature*, 2008, **451**, 652–657.
2 B. L. Ellis, K. T. Lee and L. F. Nazar, *Chem. Mater.*, 2010, **22**, 691–714.
3 A. Manthiram, *J. Phys. Chem. Lett.*, 2011, **2**, 176–184.
4 J. Cabana, L. Monconduit, D. Larcher and M. R. Palacin, *Adv. Mater.*, 2010, **22**, E170–E192.
5 P. Poizot, S. Laruelle, S. Grugeon, L. Dupont and J. M. Tarascon, *Nature*, 2000, **407**, 496–499.
6 B. Koo, H. Xiong, M. D. Slater, V. B. Prakapenka, M. Baasubramanian, P. Podsiadlo, C. S. Johnson, T. Rajh and E. V. Shevchenko, *Nano Lett.*, 2012, **12**, 2429–2435.
7 L. Zhang, H. B. Wu, S. Madhavi, H. H. Hng and X. W. Lou, *J. Am. Chem. Soc.*, 2012, **134**, 17388–17391.
8 B. Wang, J. S. Chen, H. B. Wu, Z. Wang and X. W. Lou, *J. Am. Chem. Soc.*, 2011, **133**, 17146–17148.
9 S. Ding, J. S. Chen and X. W. David Lou, *Adv. Funct. Mater.*, 2011, **21**, 4120–4125.
10 G. M. Zhou, D. W. Wang, F. Li, L. L. Zhang, N. Li, Z. S. Wu, L. Wen, G. Q. Lu and H. M. Cheng, *Chem. Mater.*, 2010, **22**, 5306–5313.

11 Q. Q. Xiong, J. P. Tu, Y. Lu, J. Chen, Y. X. Yu, Y. Q. Qiao, X. L. Wang and C. D. Gu, *J. Phys. Chem. C*, 2012, **116**, 6495–6502.
12 Z. Xiao, Y. Xia, Z. H. Ren, Z. Y. Liu, G. Xu, C. Y. Chao, X. Li, G. Shen and G. R. Han, *J. Mater. Chem.*, 2012, **22**, 20566–20573.
13 H. S. Lim, B. Y. Jung, Y. K. Sun and K. D. Suh, *Electrochim. Acta*, 2012, **75**, 123–130.
14 Y. Z. Su, S. Li, D. Q. Wu, F. Zhang, H. W. Liang, P. F. Gao, C. Cheng and X. L. Feng, *ACS Nano*, 2012, **6**, 8349–8356.
15 Y. Si, T. Ren, B. Ding, J. Y. Yu and G. Sun, *J. Mater. Chem.*, 2012, **22**, 4619–4622.
16 S. H. Ren, R. Prakash, D. Wang, V. S. K. Chakravadhanula and M. Fichtner, *ChemSusChem*, 2012, **5**, 1397–1400.
17 L. Li, T. T. Wang, L. Y. Zhang, Z. M. Su, C. G. Wang and R. S. Wang, *Chem.–Eur. J.*, 2012, **18**, 11417–11422.
18 Y. Chen, H. Xia, L. Lu and J. M. Xue, *J. Mater. Chem.*, 2012, **22**, 5006–5012.
19 A. Banerjee, R. Gokhale, S. Bhatnagar, J. Jog, M. Bhardwaj, B. Lefez, B. Hannoyer and S. Ogale, *J. Mater. Chem.*, 2012, **22**, 19694–19699.
20 Y. Zhao, J. X. Li, C. X. Wu, Y. H. Ding and L. H. Guan, *ChemPlusChem*, 2012, **77**, 748–751.
21 Q. M. Zhang, Z. C. Shi, Y. F. Deng, J. Zheng, G. C. Liu and G. H. Chen, *J. Power Sources*, 2012, **197**, 305–309.
22 Y. Ma, C. Zhang, G. Ji and J. Y. Lee, *J. Mater. Chem.*, 2012, **22**, 7845–7850.
23 S. M. Paek, E. Yoo and I. Honma, *Nano Lett.*, 2009, **9**, 72–75.
24 J. L. Gomez-Camer, J. Morales and L. Sanchez, *J. Mater. Chem.*, 2011, **21**, 811–818.
25 H. Kim, D. H. Seo, S. W. Kim, J. Kim and K. Kang, *Carbon*, 2011, **49**, 326–332.
26 Y. Chen, B. H. Song, X. S. Tang, L. Lu and J. M. Xue, *J. Mater. Chem.*, 2012, **22**, 17656–17662.
27 J. Z. Wang, C. Zhong, D. Wexler, N. H. Idris, Z. X. Wang, L. Q. Chen and H. K. Liu, *Chem.–Eur. J.*, 2011, **17**, 661–667.
28 G. Wang, T. Liu, X. Xie, Z. Ren, J. Bai and H. Wang, *Mater. Chem. Phys.*, 2011, **128**, 336–340.
29 J. Su, M. Cao, L. Ren and C. Hu, *J. Phys. Chem. C*, 2011, **115**, 14469–14477.
30 W. H. Shi, J. X. Zhu, D. H. Sim, Y. Y. Tay, Z. Y. Lu, X. J. Zhang, Y. Sharma, M. Srinivasan, H. Zhang, H. H. Hng and Q. Y. Yan, *J. Mater. Chem.*, 2011, **21**, 3422–3427.
31 X. Y. Li, X. L. Huang, D. P. Liu, X. Wang, S. Y. Song, L. Zhou and H. J. Zhang, *J. Phys. Chem. C*, 2011, **115**, 21567–21573.
32 B. J. Li, H. Q. Cao, J. Shao, M. Z. Qu and J. H. Warner, *J. Mater. Chem.*, 2011, **21**, 5069–5075.
33 B. J. Li, H. Q. Cao, J. Shao and M. Z. Qu, *Chem. Commun.*, 2011, **47**, 10374–10376.
34 L. W. Ji, Z. K. Tan, T. R. Kuykendall, S. Aloni, S. D. Xun, E. Lin, V. Battaglia and Y. G. Zhang, *Phys. Chem. Chem. Phys.*, 2011, **13**, 7170–7177.
35 C. T. Hsieh, J. Y. Lin and C. Y. Mo, *Electrochim. Acta*, 2011, **58**, 119–124.
36 D. Y. Chen, G. Ji, Y. Ma, J. Y. Lee and J. M. Lu, *ACS Appl. Mater. Interfaces*, 2011, **3**, 3078–3083.
37 S. K. Behera, *Chem. Commun.*, 2011, **47**, 10371–10373.
38 R. A. Pai, R. Humayun, M. T. Schulberg, A. Sengupta, J. N. Sun and J. J. Watkins, *Science*, 2004, **303**, 507–510.
39 G. R. Akien and M. Poliakoff, *Green Chem.*, 2009, **11**, 1083.
40 C. A. Eckert, B. L. Knutson and P. G. Debenedetti, *Nature*, 1996, **383**, 313–318.
41 T. Seki, J. D. Grunwaldt and A. Baiker, *Ind. Eng.Chem. Res.*, 2008, **47**, 4561–4585.
42 R. A. Lucky and P. A. Charpentier, *Adv. Mater.*, 2008, **20**, 1755–1759.
43 J. W. Zhang, L. H. Zhuo, L. L. Zhang, C. Y. Wu, X. B. Zhang and L. M. Wang, *J. Mater. Chem.*, 2011, **21**, 6975–6980.
44 F. Cansell and C. Aymonier, *J. Supercrit. Fluids*, 2009, **47**, 508–516.
45 D. C. Marcano, D. V. Kosynkin, J. M. Berlin, A. Sinitskii, Z. Z. Sun, A. Slesarev, L. B. Alemany, W. Lu and J. M. Tour, *ACS Nano*, 2010, **4**, 4806–4814.
46 J. Ming, C. Y. Wu, H. Y. Cheng, Y. C. Yu and F. Y. Zhao, *J. Supercrit. Fluids*, 2011, **57**, 137–142.
47 V. Chandra, J. Park, Y. Chun, J. W. Lee, I.-C. Hwang and K. S. Kim, *ACS Nano*, 2010, **4**, 3979–3986.
48 E. Kang, Y. S. Jung, A. S. Cavanagh, G.-H. Kim, S. M. George, A. C. Dillon, J. K. Kim and J. Lee, *Adv. Funct. Mater.*, 2011, **21**, 2430–2438.

